Monthly Notices
of the
ROYAL ASTRONOMICAL SOCIETY

MNRAS **496,** 3128–3141 (2020)
Advance Access publication 2020 June 20

doi:10.1093/mnras/staa1742

Characterizing the radio continuum nature of sources in the massive star-forming region W75N (B)

A. Rodríguez-Kamenetzky,[1★] C. Carrasco-González,[2] J. M. Torrelles,[3,4] W. H. T. Vlemmings,[5] L. F. Rodríguez,[2] G. Surcis,[6] J. F. Gómez,[7] J. Cantó,[8] C. Goddi,[9,10] J. S. Kim,[11] S. -W. Kim,[11] N. Añez-López,[3,4] S. Curiel[8] and H. J. van Langevelde[12,13]

[1]*Instituto de Astronomía Teórica y Experimental, (IATE-UNC), X5000BGR Córdoba, Argentina*
[2]*Instituto de Radioastronomía y Astrofísica (IRyA-UNAM), 58089 Morelia, Mexico*
[3]*Institut de Ciències de l'Espai (ICE, CSIC), Can Magrans s/n, E-08193 Cerdanyola del Vallès, Spain*
[4]*Institut d'Estudis Espacials de Catalunya (IEEC), E-08034 Barcelona, Spain*
[5]*Department of Earth and Space Sciences, Chalmers University of Technology, SE-43992 Onsala, Sweden*
[6]*INAF–Osservatorio Astronomico di Cagliari, Via della Scienza 5, I-09047 Selargius (CA), Italy*
[7]*Instituto de Astrofísica de Andalucía, CSIC, Glorieta de la Astronomía s/n, E-18008 Granada, Spain*
[8]*Instituto de Astronomía, Universidad Nacional Autónoma de México (UNAM), Apartado Postal 70-264, 04510 México, DF, Mexico*
[9]*ALLEGRO/Leiden Observatory, Leiden University, P.O. Box 9513, NL-2300 RA Leiden, the Netherlands*
[10]*Department of Astrophysics/IMAPP, Radboud University Nijmegen, P.O. Box 9010, NL-6500 GL Nijmegen, the Netherlands*
[11]*Korea Astronomy and Space Science Institute, 776 Daedeokdaero, Yuseong, Daejeon 305-348, Republic of Korea*
[12]*Joint Institute for VLBI ERIC (JIVE), Oude Hoogeveensedijk 4, NL-7991 PD Dwingeloo, the Netherlands*
[13]*Leiden Observatory, Leiden University, PO Box 9513, NL-2300 RA Leiden, the Netherlands*

Accepted 2020 June 12. Received 2020 May 19; in original form 2020 February 28

ABSTRACT

The massive star-forming region W75N (B) is thought to host a cluster of massive protostars (VLA 1, VLA 2, and VLA 3) undergoing different evolutionary stages. In this work, we present radio continuum data with the highest sensitivity and angular resolution obtained to date in this region, using the VLA-A and covering a wide range of frequencies (4–48 GHz), which allowed us to study the morphology and the nature of the emission of the different radio continuum sources. We also performed complementary studies with multi-epoch Very Large Array (VLA) data and Atacama Large Millimeter Array (ALMA) archive data at 1.3 mm wavelength. We find that VLA 1 is driving a thermal radio jet at scales of ≈0.1 arcsec (≈130 au), but also shows signs of an incipient hypercompact H II region at scales of $\lesssim$1 arcsec ($\lesssim$1300 au). VLA 3 is also driving a thermal radio jet at scales of a few tenths of arcsec (few hundred of au). We conclude that this jet is shock exciting the radio continuum sources Bc and VLA 4 (obscured Herbig–Haro objects), which show proper motions moving outward from VLA 3 at velocities of ≈112–118 km s^{-1}. We have also detected three new weak radio continuum sources, two of them associated with millimetre continuum cores observed with ALMA, suggesting that these two sources are also embedded young stellar objects in this massive star-forming region.

Key words: stars: massive – stars: protostars – H II regions – Herbig–Haro objects – ISM: jets and outflows – radio continuum: ISM.

1 INTRODUCTION

Although it is well known that the most massive stars have a great impact on the galactic environment, many aspects related to their early evolutionary stages still remain unknown. For instance, massive protostars are deeply embedded in dense molecular gas, located at typical distances of few thousand parsecs. Thus, detailed studies of these objects require observations with very high sensitivity and angular resolution. One of the best known massive star-forming regions is W75N (B), located in the Cygnus X complex at a distance of 1.3 kpc (Rygl et al. 2012), comprising of dense molecular

★ E-mail: adriana.rodriguez@unc.edu.ar

clouds (Dickel, Dickel & Wilson 1978; Persi, Tapia & Smith 2006) and showing strong maser emission of different molecular species (e.g. Baart et al. 1986; Hunter et al. 1994; Torrelles et al. 1997; Surcis et al. 2009; Krasnov et al. 2015; Colom et al. 2018). This region constitutes an excellent laboratory to study early stages of massive star formation, since it hosts a cluster of massive protostars (e.g. Shepherd, Testi & Stark 2003), probably undergoing different evolutionary phases (Torrelles et al. 1997).

Since its discovery, W75N(B) has been widely studied, revealing the presence of five radio continuum sources (named VLA 1, VLA 2, VLA 3, VLA 4, and Bc; e.g. Hunter et al. 1994; Torrelles et al. 1997; Carrasco-González et al. 2015) and a large-scale high-velocity molecular outflow (e.g. Davis et al. 1998; Shepherd et al. 2003). Among the five radio continuum sources, VLA 1 was proposed to be an evolved young stellar object (YSO), whereas VLA 2 is probably the least evolved YSO in the region (e.g. Torrelles et al. 1997). These two sources are the only ones in the region that are associated with 22 GHz water (e.g. Torrelles et al. 1997; Surcis et al. 2009, 2011, 2014; Kim et al. 2013) and 6.7 GHz methanol maser emission, which was actually detected from a location in between them (e.g. Minier, Booth & Conway 2000; Surcis et al. 2009). Furthermore, polarimetric maser observations show the presence of a magnetic field oriented in the direction of the molecular outflow (e.g. Hutawarakorn, Cohen & Brebner 2002; Surcis et al. 2009, 2011, 2014). However, despite the deep studies conducted so far towards W75N(B), the nature of some of the radio continuum sources in the region is not well known yet.

In this work, we analyse radio continuum data obtained with the Karl Jansky Very Large Array (VLA) over a wide range of frequencies (4–48 GHz), which provide images with the highest sensitivity (rms = 8 μJy per beam) and angular resolution ($0\farcs12 \times 0\farcs09$, PA = -69°) obtained to date in this region. Part of these data were presented by Carrasco-González et al. (2015), who focused their attention on the remarkable source VLA 2, reporting through radio continuum and H_2O maser observations the transition from an uncollimated outflow to a collimated outflow over a period of only 18 yr. In this work, we focus on the remaining sources in the field: VLA 1, VLA 3, VLA 4, and Bc (see Fig. 1a). These observations allow us to perform a deep multifrequency study of the morphology of the sources and of their nature. We also analyse Atacama Large Millimeter Array (ALMA) 1.3 mm continuum and spectral line archive data obtained towards this region.

2 OBSERVATIONS

2.1 VLA

The star-forming region W75N (B) was observed with the VLA of the National Radio Astronomy Observatory (NRAO)[1] in its A-configuration at *C* (6 cm), *Ku* (2 cm), *K* (1.3 cm), and *Q* (7 mm) bands (project code 14A-007). A detailed description of the observations and calibration procedures can be found in Carrasco-González et al. (2015). Deconvolved images were obtained with the task CLEAN of the Common Astronomy Software Applications (CASA,[2] version 4.1.0) data reduction package, using multifrequency synthesis (parameter nterms = 2) and multiscale cleaning (Rau & Cornwell 2011). Primary beam corrections were applied. We split each band data set to build images of narrower bandwidth (1 and 2 GHz), using different weightings, i.e. natural, uniform, and Briggs (Briggs 1995) to achieve the best compromise between sensitivity and angular resolution, depending on the analysis performed (e.g. spectral energy distributions, angular size versus frequency). We also made a single image combining all four bands (*C*, *Ku*, *K*, and *Q*; Fig. 1), as well as individual images integrating the full bandwidth of each frequency band (Fig. 2). Moreover, the multifrequency synthesis cleaning technique allows us to obtain a spectral index map covering the entire range of the observed frequencies.

All the radio continuum images presented in this paper, as well as the spectral energy distribution (SED) analysis of the different sources are based on the VLA project code 14A-007 (epoch 2014.29). However, in order to study the kinematics of some of the sources in the region (VLA 4 and Bc) we also reanalysed previously reported, multi-epoch VLA archive data (project codes AT141, AF381, and AS831; see Carrasco-González et al. 2010, for details on the observations). This, along with our new *K*-band observations, allow us to compute proper motions in a period spanning 22 yr, from 1992 to 2014. Calibration of these archive data was undertaken following standard VLA procedures, using the Astronomical Image Processing System (AIPS)[3] data reduction package.

Parameters of the data sets and images are summarized in Tables 1 and A1, respectively.

2.2 ALMA

W75N (B) was observed with ALMA at 1.3 mm during three sessions, on 2018 May 6th, 7th, and 11th (archive ALMA data, project code: 2017.1.01593.S). In total, approximately 16 min were spent on source. During the session on May 7th, only 1 min of useful data on W75N (B) was obtained. The phase centre for the W75N (B) observations was RA(J2000) = 20:38:37.0 and Dec(J2000) = + 42:37:51.0, which is ∼18 arcsec north of the VLA 1–VLA 2–VLA 3 sources. As a result, the mm continuum sources discussed in this work are detected towards the edge of the ALMA primary beam (FWHM ≃ 27 arcsec). The ALMA images presented in this paper (Section 3.2) have not been corrected by primary beam but they are of good enough quality for the identification of different mm continuum sources. The observations were performed using four spectral windows (spws). Two spws had 1.875 GHz bandwidth and were centred on 217.117 and 230.552 GHz. Two further spws had 117.188 MHz bandwidth and were centred at 216.124 and 231.334 GHz. All spws had 1920 spectral channels after hanning smoothing. During the observations, 46 ALMA telescopes participated, with a minimum baseline length of 15 m and a maximum baseline length of 500 m. This resulted in a maximum recoverable scale of ∼7 arcsec.

The observations were initially calibrated using the ALMA pipeline of CASA 5.1.1 (McMullin et al. 2007). Subsequently, after excluding the channels showing line emissions, we performed two interactions of phase self-calibration on the continuum emission by using CASA 5.1.1. This improved the continuum signal-to-noise ratio by a factor of three. Next, the data were imaged and cleaned (task TCLEAN) centred on VLA 2, using Briggs weighting with a robust parameter of 0.5, yielding a synthesized beam size for the 1.3 mm continuum observations of $1\farcs73 \times 0\farcs86$ with a position angle of -4° (Fig. 3).

[1]NRAO is a facility of the National Science Foundation operated under cooperative agreement by Associated Universities, Inc.
[2]https://science.nrao.edu/facilities/vla/data-processing
[3]http://www.aips.nrao.edu/index.shtml

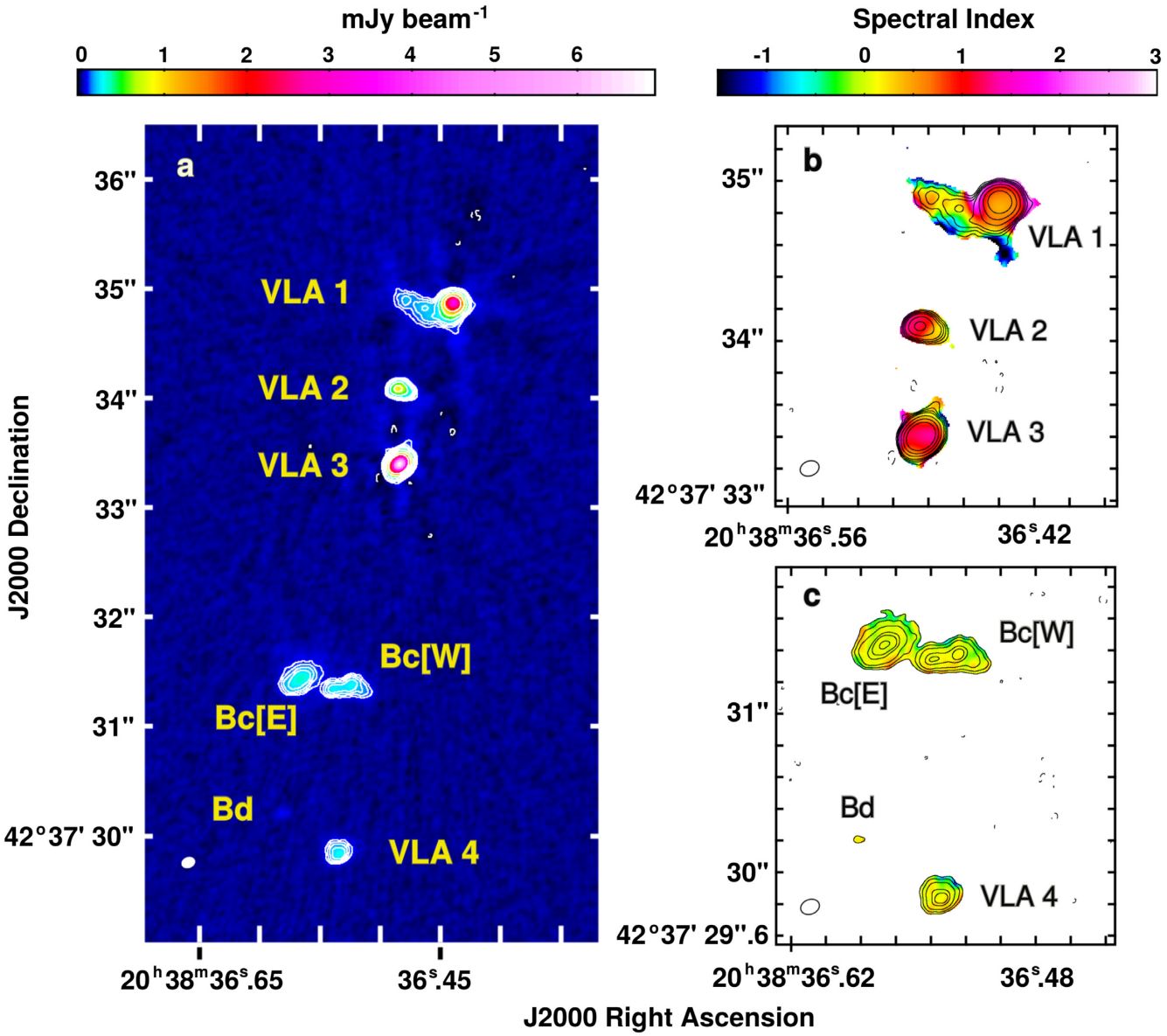

Figure 1. Radio continuum image and spectral index maps of W75N (B) made by the combination of *C*, *Ku*, *K*, and *Q* bands (epoch 2014.29), using multifrequency synthesis cleaning and Briggs weighting (robust 0). (a) Continuum image: contours are −4, 9, 13, 18, 25, 50, 100, and 200 times the rms, 8 μJy per beam. Panels (b) and (c) show a close-up of the northern region containing sources VLA 1, 2, and 3, and the southern region containing sources Bc and VLA 4, respectively. In both cases, intensity contours of panel (a) are shown over the spectral index map (colour scale). The pixels shown in spectral index maps are those with S/N > 7 in the continuum image. Synthesized beam $= 0\farcs12 \times 0\farcs09$ (PA $= -69°$).

3 RESULTS

3.1 VLA

The most recent data set (epoch 2014.29, see Table A1) provides radio continuum images of W75N (B) with unprecedented sensitivity. Also, these observations enable us to perform a detailed study of different structures associated with the sources and their emission nature within several ranges of frequencies.

By combining data from all the observed bands (epoch 2014.29), we obtain the hitherto deepest (rms $\simeq$ 8 μJy per beam; beam $= 0\farcs12 \times 0\farcs09$, PA $= -69°$) radio continuum image of this region, and a spectral index map (Fig. 1). All the previously known sources in the field (VLA 1, VLA 2, VLA 3, VLA 4, and Bc) are labelled in Fig. 1(a).

In Fig. 2, we show the images of the radio continuum sources at *C*, *Ku*, *K*, and *Q* bands, covering the entire bandwidth in each case (see Table A1 for the image parameters). Due to spatial filtering effects that worsen at increasing frequency for a given configuration, *C* and *Ku* bands are more sensitive to extended emission than *K* and *Q* bands, which tend to favour the detection of compact structures. Taking this into account, and given the wide frequency coverage of our observations, both extended and compact emission of the sources can be studied with high sensitivity. We note that all the sources are detected with an S/N ratio much higher than 5 from *C* to *K* band (Figs 2a, b, and c). However, at the highest frequency (*Q* band in Fig. 2d), only the northern radio sources are detected, with Bc and VLA 4 hardly distinguishable from the noise. The flux densities of VLA 1, VLA 3, VLA 4, and Bc at each band are listed

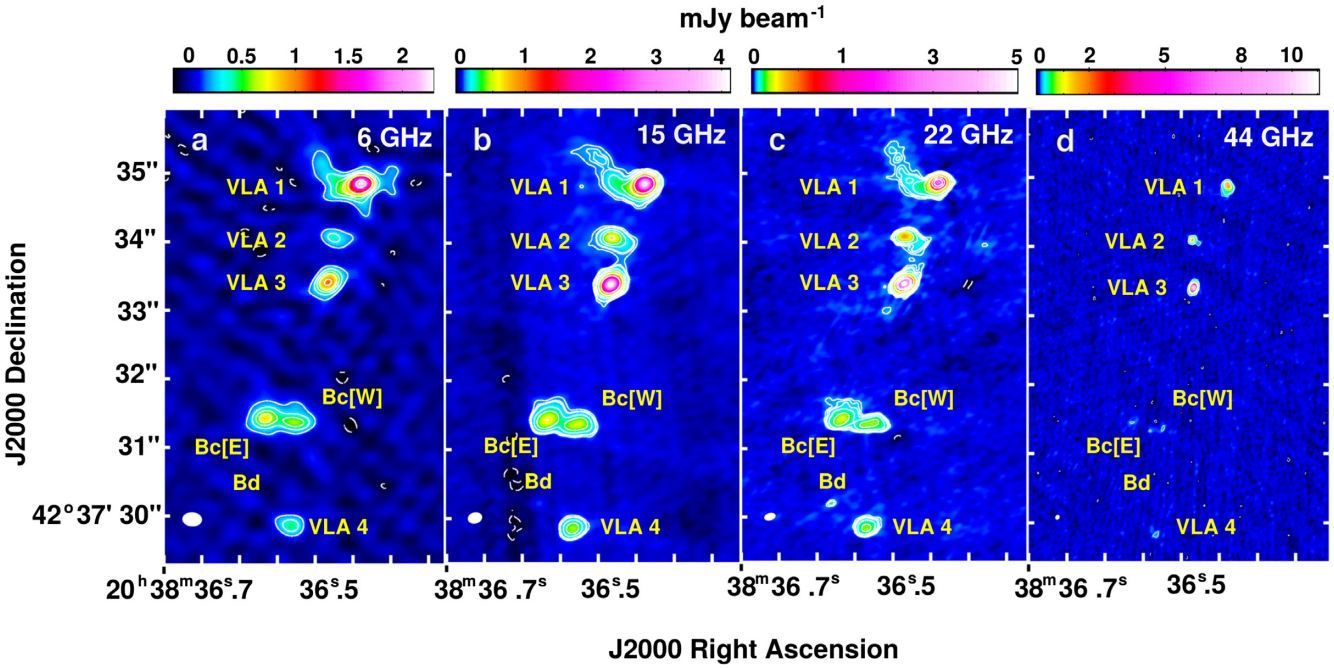

Figure 2. Radio continuum images of W75N (B) at *C* (6 GHz), *Ku* (15 GHz), *K* (22 GHz), and *Q* (44 GHz) bands (epoch 2014.29) are shown in panels a, b, c, and d, respectively. White dashed and solid contours represent negative and positive values, respectively, corresponding to different sigma levels: −3, 5, 10, 15, 20, 30, and 60 times 30 μJy per beam (6 GHz image, uniform weighting); −4, 5, 7, 8, 15, 25, 50, 100, and 300 times 10 μJy per beam (15 GHz image, natural weighting); −4, 5, 7, 9, 15, 30, 100, 200, 300, and 600 times 10 μJy per beam (22 GHz image, natural weighting); −3, 5, 10, 30, 50, 100, 300, and 500 times 20 μJy per beam (44 GHz image, natural weighting). In each panel, the synthesized beam is indicated with a white ellipse at the bottom left.

Table 1. Parameters of the VLA observations.

Project	Observation date	Configuration	Central frequency (GHz)	Flux calibrator	Phase calibrator
AT141[a]	1992 Nov 24 (1992.9)	A	8.44	3C 48	J2007+4029
AF381[a]	2001 Apr 23 (2001.31)	B	15.0	3C 286	J2015+371
AS831[a]	2006 May 18 (2006.38)	A	8.46	3C 286	J2007+4029
14A-007[b]	2014 March 15 (2014.29)	A	6.0	3C 286	J2007+4029
14A-007[b]	2014 March 15 (2014.29)	A	15.0	3C 286	J2007+4029
14A-007[b]	2014 March 15 (2014.29)	A	22.0	3C 286	J2007+4029
14A-007[b]	2014 March 15 (2014.29)	A	44.0	3C 286	J2007+4029

Notes. [a]Archive data.
[b]Partially reported by Carrasco-González et al. (2015).

in Table 2 (a detailed discussion of the parameters of VLA 2 is given in Carrasco-González et al. 2015).

In addition to all these sources, three new weak (<100 μJy, see Table 2) compact radio continuum sources are detected in the images at *Ku* and *K* bands, as well as in the image obtained by combining all four bands. These new sources are located ∼8 arcsec north-east (VLA [NE]) and ∼6 arcsec south-west (VLA [SW]) from VLA 2, and ∼0.5 arcsec north-east (Bd) from VLA 4. Figs 3 and A1 show the position and contour maps, respectively, of these weak radio sources.

3.2 ALMA

The ALMA continuum observations at 1.3 mm show four cores in a region of ∼14 arcsec (MM1, MM2, MM3, and MM[N]; Fig. 3). Three of them (MM1, MM2, and MM3) have been previously identified by Minh et al. (2010) with the Submillimeter Array (SMA) at 217 and 347 GHz, with angular resolution similar to that in our ALMA images. The fourth millimetre core, MM[N], is located ∼9 arcsec north from MM1 and has not been previously reported. We did not detect with the VLA any radio continuum source towards MM[N], with an upper limit of ∼30 μJy (4σ in the combination of $C + Ku + K + Q$ bands; Table A1). From Fig. 3, we see that the massive protostars VLA 1, VLA 2, and VLA 3 are associated with the brightest millimetre core, MM1, although the limited angular resolution of the ALMA observations (1.″73 × 0.″86, PA = −4°) and the north–south distribution of the sources (with a maximum angular separation among them of $\lesssim$1.5 arcsec), prevent us from distinguishing the contribution of the individual sources to the total dust emission of MM1. On the other hand, two of the newly identified VLA radio continuum sources, VLA[SW] and VLA[NE] (Section 3.1; Figs 3 and A1), are associated with MM2 and MM3, respectively, indicating they are embedded YSOs. However, the fact that Bc, VLA 4, and Bd are not clearly associated with any millimetre continuum core suggests

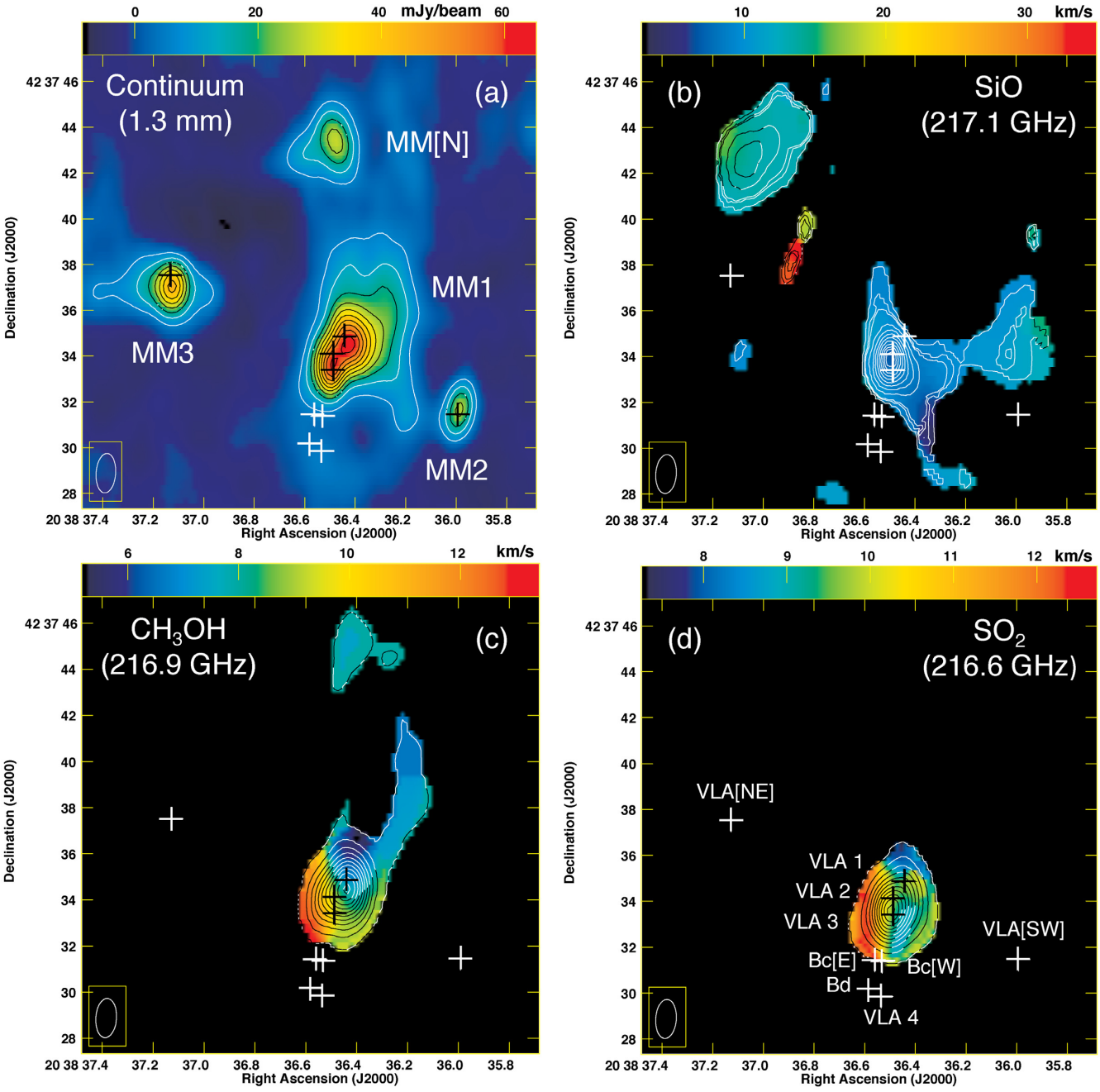

Figure 3. (a) Colour image and contour map of the continuum emission at 1.3 mm. Contour levels are 1, 2, 3, 4, 5, 6, 7, 8, 9, and 10 × 6.1 mJy beam^{-1}. The mm sources MM1, MM2, and MM3 are labelled (nomenclature by Minh et al. 2010). A new mm source detected with ALMA ∼9 arcsec north from MM1 is labelled as MM[N]. Crosses indicate the positions of the radio continuum sources at cm wavelengths identified with the VLA (this work). (b) Contour map of the integrated intensity and velocity field colour image (moment of order 1) of the SiO (217.1 GHz) line. Contour levels are 0.4, 0.8, 1, 2, 3, 4, 5, 6, 7, 8, 9, and 10 × 0.27 Jy beam^{-1} km s^{-1}. (c) Same as the previous panel but for the CH_3OH (216.9 GHz) line. Contour levels are 0.1, 1, 2, 3, 4, 5,6, 7, 8, 9, and 10 × 0.6 Jy beam^{-1} km s^{-1}. (d) Same as the previous panel but for the SO_2 (216.6 GHz) line. Contour levels are 0.1, 1, 2, 3, 4, 5, 6, 7, 8, 9, and 10 × 0.8 Jy beam^{-1} km s^{-1}. Primary beam corrections have not been applied to these images, given that the mm cores are detected at the edge of the ALMA primary beam (FWHM ≃ 27 arcsec; see Section 3.2). Assuming that the ALMA primary beam can be approximated by a Gaussian function, the intensities given in these images should be corrected by factors of ∼4, 10, 2, and 1.4 at the positions of MM1, MM2, MM3, and MM[N], respectively.

that they are probably not YSOs (see Section 4.3 for the discussion, in particular, on the nature of the Bc and VLA 4 radio continuum sources).

Because these millimetre continuum cores are found at the edge of the ALMA primary beam and they were only observed at a single frequency band, we are not able to derive with accuracy their physical parameters with the present data. For those estimates, we refer to Minh et al. (2010).

In Fig. 3, we also show the images of the integrated intensity and velocity field (first-order momentum) of the molecular lines CH_3OH [5(1,4)–4(2,2); rest frequency 216.94552 GHz], SO_2 [22(2,20)-22(1,21); 216.64330 GHz], and SiO [$v = 0$ (5-4); 217.10498 GHz]

Table 2. Integrated flux densities of the radio sources detected in epoch 2014.29.

Source	S_C (mJy)	S_{Ku} (mJy)	S_K (mJy)	S_Q (mJy)	S_{CKuKQ} (mJy)
VLA 1	3.8 ± 0.3	5.5 ± 0.3	5.8 ± 0.1	5.2 ± 0.3	6.0 ± 0.2
VLA 3	1.6 ± 0.1	5.2 ± 0.2	7.7 ± 0.1	15.7 ± 0.8	9.06 ± 0.07
VLA 4	0.67 ± 0.05	0.76 ± 0.05	0.83 ± 0.05	0.53 ± 0.08	0.69 ± 0.04
Bc[E]	1.9 ± 0.2	1.8 ± 0.3	1.9 ± 0.3	<0.080	1.5 ± 0.2
Bc[W]	1.7 ± 0.2	1.5 ± 0.2	1.4 ± 0.3	<0.080	1.4 ± 0.3
Bd	<0.1	0.02 ± 0.01	0.09 ± 0.02	<0.080	0.06 ± 0.01
VLA[SW]	<0.1	0.09 ± 0.01	0.11 ± 0.02	<0.080	0.09 ± 0.01
VLA[NE]	<0.1	<0.052	0.03 ± 0.03	<0.080	0.041 ± 0.008

Note. Flux density upper limits correspond to 4σ. Errors are computed as the quadratic sum of both calibration and fitting error, except in the case of the last column, S_{CKuKQ}, which correspond to fitting errors. See Table A1 for image details.

as observed with the ALMA archive data. A main molecular core centred on VLA 1–VLA 2–VLA 3 is detected through the CH_3OH and SO_2 lines. This molecular core, of ∼4 arcsec (∼5200 au) size, exhibits a velocity gradient of ∼5 km s^{-1} along the north-west–south-east direction, which is fully consistent with the velocity gradient reported by Minh et al. (2010) in H_2CO with the SMA (∼1 km s^{-1} arcsec^{-1}). Given their angular resolution, these ALMA observations (and the SMA observations; Minh et al. 2010) cannot resolve the structure and motions of the dust and molecular gas around each of the individual sources VLA 1, VLA2, and VLA 3.

On the other hand, the SiO emission shows an irregular distribution covering a broader velocity range ($V_{LSR} \approx$ 10–35 km s^{-1}) than CH_3OH and SO_2 (Fig. 3), with the highest velocity emission ($V_{LSR} \approx$ 30–35 km s^{-1}) located ∼6 arcsec north-east from VLA 1–VLA 2–VLA 3. This high-velocity SiO emission could be tracing outflow motions driven by any of the central VLA sources. ALMA observations with higher angular resolution are clearly necessary to identify, isolate, and study the expected different dust and molecular gas components around the individual massive protostars.

4 NATURE OF THE INDIVIDUAL RADIO SOURCES

4.1 VLA 1

It can be seen from Figs 1 and 4 that VLA 1 exhibits a tail-shaped extended component. This is the first time that this particular structure is observed in VLA 1, due to the high sensitivity of our images. In Fig. 1(b), we show the spatial distribution of spectral indices (α, defined as $S_\nu \propto \nu^\alpha$) along the source, covering the whole range of frequencies. It can be noticed that the central region of VLA 1 presents positive spectral indices (∼+0.5, measured from the spectral index map, at the continuum emission peak), while the tail-shaped structure is dominated by a flat spectrum with $\alpha \simeq 0$.

By studying the emission at different bands, we can see that the morphology of the VLA 1 source seems to be composed by an extended and a compact components (see Fig. 4). At the lowest frequencies (15 and 22 GHz), the higher optical depth and lower angular resolutions emphasize the extended component. In Figs 4(a) and (b), we can clearly see a 'cometary' tail curved in the north-east direction. As we go to higher frequencies (44 GHz), the higher angular resolution and lower optical depth allow us to filter out most of the low brightness extended emission, and the most compact higher brightness emission is resolved into an elongated source in the NE–SW direction (PA = +42° ± 5°; see Figs 4c and d).

To study the emission nature of both, the extended and the compact components of VLA 1, we compute the SED of the source in the whole range of observed frequencies with low angular resolution, and the SED at *Q* band (where most of the extended emission is filtered) with high angular resolution. In Fig. 5 (top panel), we show the SED over the entire range of frequencies, obtained by measuring flux densities in images with 2 GHz bandwidth, using uniform weighting for *C* band and natural weighting for *Ku*, *K*, and *Q* bands. All images were convolved to 0.″37, corresponding to the lowest resolution in *C* band. Flux densities were determined by a Gaussian fit within a circular region of 1.25 arcsec diameter enclosing the source. We note that these data were observed with the telescope array same configuration, and in this case, the largest scales in the images could be more heavily filtered at high frequencies, which could result in spuriously lower values of the spectral index. However, we limited the study of the low angular resolution SED to the core of the emission, which has a size of ∼400 mas. Emission with this size is fully recovered at all bands. Just for description purposes, we have performed a fit to the observed flux densities from 4 to 47 GHz through an ad hoc function $S_\nu = a\nu^\alpha\ [1-e^{-b/\nu^\beta}]$ (Fig. 5, top panel). The fit gives $a = 0.62$, $\alpha = 1.38$, $b = 13.29$, and $\beta = 1.42$, with S_ν in mJy and ν in GHz. Within the uncertainties in the observations, this SED is consistent with an H II region thermal bremsstrahlung spectrum, opaque at low frequencies ($\lesssim$10 GHz) and optically thin at high frequencies ($\gtrsim$20 GHz). The size of the extended emission, including the tail, is of the order of 1 arcsec, corresponding to an extension of ∼0.006 pc. This size is significantly smaller than 0.1 pc, suggesting it could be classified as a hypercompact (HC) H II region, according to Kurtz (2005).

We want to note, however, that we cannot rule out the possibility that some dust contribution from the extended emission in VLA 1 is present at *Q* band (Figs 4a and b). If this were true, the real SED of the ionized gas would be flatter at high frequencies than that shown in Fig. 5 (top panel). In any case, as stated in Section 3.2, very high angular resolution observations with ALMA are clearly needed to individually resolve the dust content of each YSO in the region.

In order to study VLA 1 with as less contribution as possible from the extended emission, we measured flux densities with very high angular resolution in eight R0-weighted (Briggs weighting using parameter robust = 0) images of 1 GHz bandwidth within the *Q* band (see Table A1 for image details). All flux densities are measured within a circular region of 0.16 arcsec diameter enclosing the source. The resulting SED is shown at the bottom panel of Fig. 5. Applying a linear fit to this SED, we obtain a spectral index $\alpha = +0.5 \pm 0.4$, consistent with partially optically thick free–free emission from

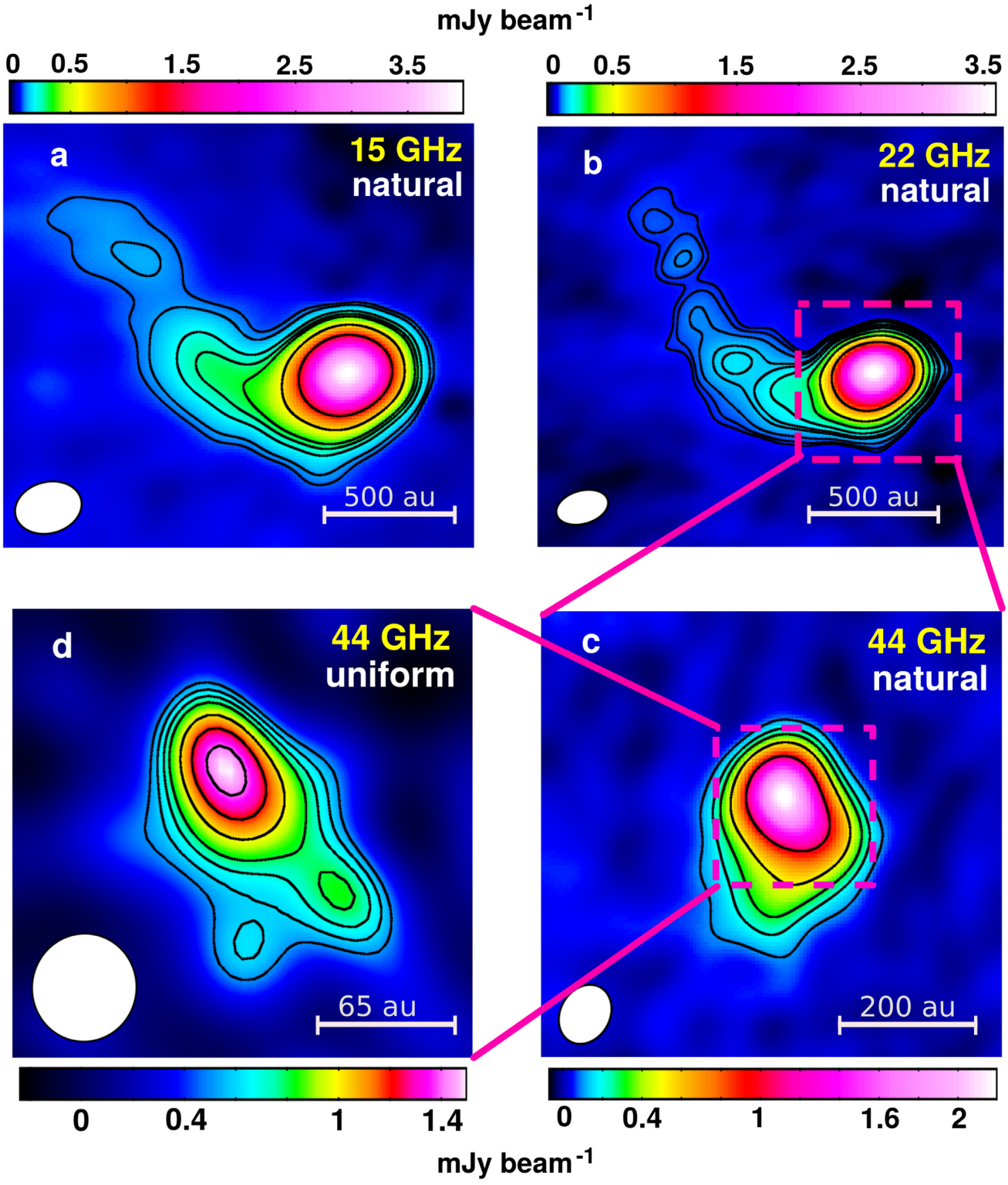

Figure 4. VLA 1 continuum emission (epoch 2014.29). (a) Natural-weighted image at *Ku* band (central frequency 15 GHz); contours are −3, 6, 8, 15, 20, 25, 50, and 100 × 10 μJy per beam, the rms of the map. The synthesized beam is 0.″21 × 0.″16, PA = −75°. (b) Natural-weighted image at *K* band (central frequency 22 GHz); contours are −3, 6, 7, 9, 13, 15, 20, 30, 50, 100 × the rms = 10 μJy per beam. The synthesized beam is 0.″16 × 0.″10, PA = −74°. The magenta dotted rectangle indicates the zoomed-in region shown in panel (c). (c) Natural-weighted image at *Q* band (central frequency 44 GHz); contours are −3, 5, 10, 15, 25, 50 × the rms = 20 μJy per beam. The synthesized beam is 0.″07 × 0.″05, PA = −29°. The magenta dotted rectangle indicates the zoomed-in region shown in panel (d). (d) Uniform-weighted image at *Q* band; contours are −3, 5, 6, 7, 8, 10, 12, 14 × the rms = 100 μJy per beam. The synthesized beam is 0.″038 × 0.″037, PA = −9°. The physical scale of 65 au corresponds to 0.05 arcsec.

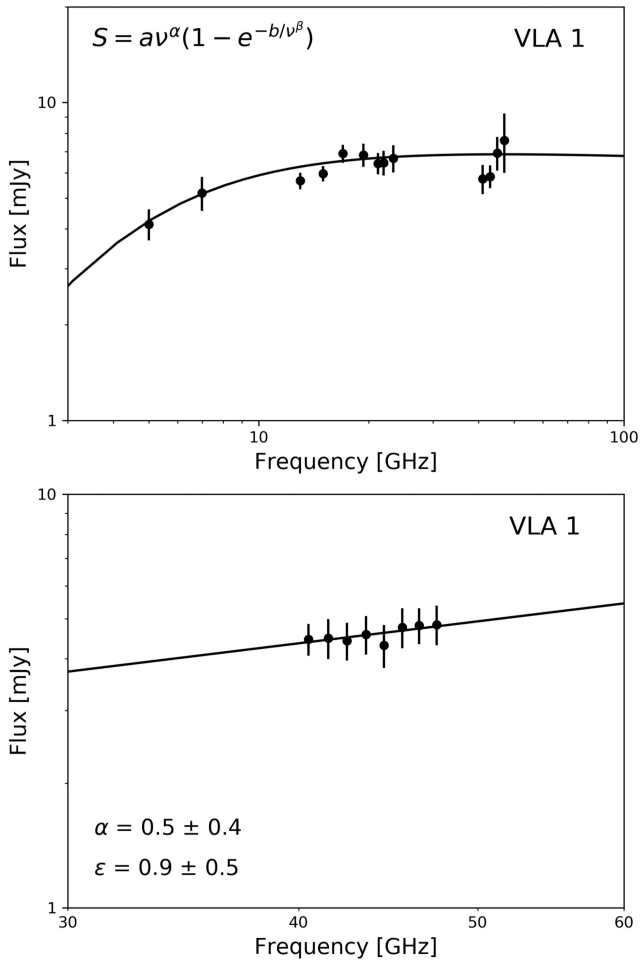

Figure 5. VLA 1 SED (epoch 2014.29). Top panel: the SED is computed in the whole range of observed frequencies. Flux densities are obtained from Gaussian fits to 2 GHz bandwidth images within a circular region of 1.25 arcsec diameter enclosing the source. We use uniform weighting at *C* band and natural weighting at *Ku*, *K*, and *Q* bands. A fit to the measured flux densities is also shown ($S_\nu = a\nu^{\alpha}\ [1-e^{-b/\nu^{\beta}}]$, with $a = 0.62$, $\alpha = 1.38$, $b = 13.29$, and $\beta = 1.42$, with S_ν in mJy and ν in GHz). This fitted ad hoc function is only for description purposes of the observed SED (see Section 4.1). Bottom panel: Spectrum at *Q* band. Flux densities are obtained from Gaussian fits to 1 GHz bandwidth images within a circular region of 0.16 arcsec diameter. We use Briggs weighting (robust 0). The solid line is a linear least-squares fit to the log data, from which we derive a spectral index $\alpha = +0.5 \pm 0.4$ that correspond to $\epsilon = +0.9 \pm 0.5$, consistent with a thermal radio jet (see Section 4.1). All data points are shown with measurement errors, considering both fitting and calibration uncertainties. Note that these panels trace different components in the source: while the top panel corresponds to the HCH II region, the bottom one traces the compact jet.

a thermal radio jet, as predicted by models given by Reynolds (1986), and consistent with typical values measured for thermal radio jets (e.g. Anglada, Rodríguez & Carrasco-González 2018). This is also in agreement with previous works by Baart et al. (1986) and Torrelles et al. (2003), who detected the presence of a radio jet traced by the distribution of OH and H_2O masers, respectively, along the same direction as the radio continuum emission (PA $\approx +43^\circ$, Torrelles et al. 1997, 2003). According to Reynolds models, the distance to the driving source where the jet becomes optically thin varies with frequency as a power law. This distance is interpreted as the angular size of the semimajor axis of the jet, θ_ν. Therefore, $\theta_\nu \propto \nu^{-0.7/\epsilon}$, where the index ϵ is related to the spectral index α as $\alpha = 1.3 - 0.7/\epsilon$ in the case of an isothermal jet with constant velocity and ionization fraction. Thus, from the SED in *Q* band we derive $\epsilon = +0.9 \pm 0.5$, suggesting a conical jet ($\epsilon = 1$).

All these results indicate that VLA 1 might consist of a thermal radio jet surrounded by an HCH II region. Assuming this is the case, we can estimate the mass-loss rate and some parameters of the H II region. In order to estimate the protostar mass-loss rate $\dot{M}$, we follow equation (3) from Beltrán et al. (2001) based on the model from Reynolds (1986):

$$\frac{\dot{M}}{10^{-6}\ \mathrm{M_\odot\ yr^{-1}}} = 0.108 \left[\frac{(2-\alpha)(\alpha+0.1)}{1.3-\alpha}\right]^{0.75} \times \left[\left(\frac{S_\nu}{\mathrm{mJy}}\right)\left(\frac{\nu}{10\ \mathrm{GHz}}\right)^{-\alpha}\right]^{0.75} \left(\frac{d}{\mathrm{kpc}}\right)^{1.5} \left(\frac{\nu_t}{10\ \mathrm{GHz}}\right)^{0.75\alpha-0.45} \times \left(\frac{\theta_\mathrm{o}}{\mathrm{rad}}\right)^{0.75} \left(\frac{T_\mathrm{e}}{10^4\ \mathrm{K}}\right)^{-0.075} (\sin i)^{-0.25} \left(\frac{V_\mathrm{jet}}{200\ \mathrm{km\ s^{-1}}}\right)\left(\frac{1}{x_\mathrm{o}}\right), \quad (1)$$

where S_ν is the flux density at the frequency ν, α the spectral index, $\theta_\mathrm{o} = 0.88$ rad the jet injection opening angle, estimated as $\theta_\mathrm{o} = 2\arctan(\theta_\mathrm{min}/\theta_\mathrm{maj})$, where θ_min and θ_maj are the deconvolved minor and major axes of the Gaussian fit to the source, respectively. $T_\mathrm{e} = 10^4$ K is the electron temperature, x_o the ionization fraction, V_jet the jet velocity, i the jet inclination angle, ν_t the turnover frequency, and $d = 1.3$ kpc the distance to the region W75N (B). The values of ν and S_ν correspond to the *Q*-band image, being $\nu = 44$ GHz the central frequency of the band and $S_\nu = 15.7 \pm 0.1$ mJy. The spectral index $\alpha = +0.5 \pm 0.4$ is derived from a linear fit to the SED (see Fig. 5, bottom panel), from which we can also infer that the jet emission is partially optically thick up to $\nu = 47$ GHz. Thus, we take this value as a lower limit to the turnover frequency ν_t (above which the entire jet becomes optically thin). Since we cannot specify the jet inclination angle i, we adopt $i = 45^\circ$, as variations from 45° to 90° only change the mass-loss estimate by less than 10 per cent. Moreover, both the ionization fraction and the jet velocity are unknown. Typical values for V_jet range from 100 to 1000 km s^{-1}, while the ionization fraction is usually assumed to be 10 per cent (e.g. Anglada et al. 2018) for low-mass protostars. However, this value is very uncertain, and could probably be higher for high-mass protostars. According to this, we estimate lower and upper limits for the mass-loss rate of $\sim 3.5 \times 10^{-7}$ M$_\odot$ yr^{-1} (assuming $x_\mathrm{o} = 1$ and $V_\mathrm{jet} = 100$ km s^{-1}) and $\sim 3.5 \times 10^{-5}$ M$_\odot$ yr^{-1} (assuming $x_\mathrm{o} = 0.1$ and $V_\mathrm{jet} = 1000$ km s^{-1}), respectively.

On the other hand, we can obtain some estimates of the physical parameters of the H II region using data from *C* to *K* bands. Derived parameters are presented in Table 3. Within the Rayleigh–Jeans regime, the brightness temperature T_B can be written in terms of the flux density S_ν at frequency ν, and the solid angle subtended by the source Ω_S, as $T_\mathrm{B} = \frac{S_\nu c^2}{2k\nu^2\Omega_\mathrm{S}}$. The solid angle Ω_S of the elliptical Gaussian fitted to the source brightness profile is calculated as $(\pi/4\ln 2) \times \mathrm{FWHM_{maj}} \times \mathrm{FWHM_{min}}$. At the central frequency of each band, T_B is always small compared with the electronic temperature T_e, assumed to be of the order of 10^4 K for an H II region (since this is the temperature at which hydrogen ionizes). Knowing the brightness temperature, the optical depth τ_ν can be calculated from $T_\mathrm{B} = T_\mathrm{e}(1 - e^{-\tau_\nu})$. As the H II region is more optically thin at the *K* band, we choose this band to estimate some parameters. Assuming the ionization number equals the recombination number, we can estimate the ionizing photon rate $\dot{N}$, i.e. the number of ionizing photons $\lambda < 912$ Å; per unit of time, necessary to account

Table 3. VLA 1 parameters from *K*-band emission.

Parameter	Value	Description
ν	22×10^9 Hz	Band central frequency
S_ν	(5.6 ± 0.2) mJy	Flux density
$\mathrm{FWHM_{min}}$	(74 ± 3) mas $= (3.6 \pm 0.2) \times 10^{-7}$ rad	Source minor axis
$\mathrm{FWHM_{maj}}$	(100 ± 2) mas $= (4.8 \pm 0.1) \times 10^{-7}$ rad	Source major axis
L	$\sim$90 mas $\simeq$110 au	Source characteristic size
Ω_ν	$(2.0 \pm 0.2) \times 10^{-13}$ sr	Subtended solid angle
T_B	(1890 ± 10) K	Brightness temperature
τ_ν	$\sim$0.2	Optical depth
EM	$\sim 4 \times 10^8$ cm^{-6}pc	Emission measure
n_e	$\sim 10^6$ cm^{-3}	Electron number density
$\dot{\mathrm{N}}$	$\sim 6 \times 10^{44}$ photons s^{-1}	Ionizing photon rate

Note. The flux density S, $\mathrm{r_{min}}$, $\mathrm{r_{maj}}$, and the characteristic size L correspond to values derived from a bi-dimensional Gaussian fit to VLA 1 at *K* band (robust 0 weighting).

for the emission observed at *K* band:

$$\dot{\mathrm{N}} = \frac{4}{3}\pi \left(\frac{L}{2}\right)^3 n_\mathrm{e} n_\mathrm{p} \eta, \quad (2)$$

where $\eta = 3 \times 10^{-13}$ cm^3 s^{-1} the 'case B' recombination coefficient (i.e. the number of recombinations per unit time, volume, and electron and ion density) to levels $\geq$2 for $T_\mathrm{e} \approx 10^4$ K; n_e and n_p are, respectively, the number density of electrons and protons (assumed to be the same), and L is the characteristic size of the region (estimated as the geometric mean of the source major and minor axes). Assuming a homogeneous, spherical H II region of depth L, n_e can be expressed in terms of the emission measure (EM) and the geometrical depth as $n_\mathrm{e} = (\mathrm{EM/L})^{1/2}$ (with $\mathrm{EM} = \int_0^L n_\mathrm{e} n_\mathrm{p}\, \mathrm{d}l$ which, in the case of a homogeneous ionized hydrogen medium of depth L approximates to $\mathrm{EM} \simeq n_\mathrm{e}^2 L$). In turn, EM can be derived from the expression of the optical depth as $\mathrm{EM[cm^{-6}\ pc]} = 12.2 \tau_\nu [T_\mathrm{e}/\mathrm{K}]^{1.35} [\nu/\mathrm{GHz}]^{2.1}$. Thus, computing S_ν, Ω, T_B, τ_ν, L, n_e, and EM, at the central frequency of band *K* (Table 3), we finally obtain an ionizing photon rate $\dot{\mathrm{N}} \approx 6 \times 10^{44}$ photons s^{-1}. This value is much lower than typical estimations for O-B stars ($\approx 10^{48}$ photons s^{-1}). Moreover, characteristic values of EM and electron number density for HCH II regions are $\mathrm{EM} \gtrsim 10^{10}$ pc cm^{-6} and $n_\mathrm{e} \gtrsim 10^6$ cm^{-3}, respectively (Kurtz 2005). In the case of VLA 1, the electron number density we obtain is of the same order of typical values for HCH II regions, while the EM is about two orders of magnitude lower (see Table 3).

Mass-loss rates in the range of 10^{-10} (for low-mass YSOs) to 10^{-5} M$_\odot$ yr^{-1} (for high-mass YSOs) have been determined in the literature (see Anglada et al. 2018, and references therein). Thus, our estimates for the mass-loss rate of VLA 1, together with the physical parameters we obtain for the H II region, lead us to conclude that VLA 1 might be a massive protostar driving a thermal radio jet, which seems to be at the very beginning of the photoionization stage. The presence of a radio jet coexisting with an UCH II has been also reported in the massive YSOs G35.20−074N (Beltrán et al. 2016) and G345.4938+01.4677 (Guzmán et al. 2016).

4.2 VLA 3

VLA 3 was previously proposed to be a partially optically thick compact H II region (e.g. Torrelles et al. 1997; Shepherd, Kurtz & Testi 2004), but it was later suggested to be a thermal radio jet with a spectral index $\alpha_{3.6-2\mathrm{cm}} = +0.6 \pm 0.1$ (Carrasco-González et al. 2010). In our data (Figs 1 and 2), VLA 3 appears as an elongated source, with its major axis oriented in the north-west–south-east direction at all wavelengths, with a position angle $\mathrm{PA} = -17^\circ \pm 2^\circ$ (Fig. 1). The ionized emission is characterized by a spectral index $\alpha \simeq +1$ in the central region of VLA 3 (Fig. 1b), consistent with partially optically thick free–free emission. Its elongated shape and its spectral index suggest that VLA 3 could be a thermal radio jet. Thus, according to theoretical models given by Reynolds (1986), we expect to find that both the SED and the jet angular size depend on the observed frequency as power laws (see Section 4.1). Therefore, we measured the flux densities and angular sizes in several images of 2 GHz bandwidth each, covering a frequency range from 7 to 48 GHz. Flux densities are measured within a circular region of 0.5 arcsec diameter in each image, and the angular sizes correspond to the deconvolved major axis of the bi-dimensional Gaussian fit to the emission. Sizes vary in the range 30–200 mas, and therefore we can rule out that a significant amount of extended emission is filtered out at the highest frequencies. In Fig. 6, we can see that both the angular size θ_ν (top panel) and the SED (bottom panel) do vary as power laws of the frequency. In the ideal case of a conical thermal jet, with constant velocity, temperature, and ionization fraction, values of $+0.6$ and -0.7 are expected for the spectral index and the slope of the size versus frequency, respectively (Reynolds 1986). In our case, the behaviour of the size with frequency is consistent with a conical jet, while the slightly larger value of the spectral index would indicate some deviation from the ideal physical conditions.

These results support that VLA 3 is associated with a thermal radio jet as previously proposed by Carrasco-González et al. (2010). Therefore, in order to estimate the protostar mass-loss rate $\dot{M}$ we follow equation (1). In this case ν, S_ν, and α correspond to the combined image ($C + Ku + K + Q$ bands), being $\nu = 26$ GHz the central frequency of the band, $S_\nu = 9.06 \pm 0.07$ mJy, and $\alpha = +1.27$ (computed from the spectral index map at the continuum emission peak). From the SED (bottom panel of Fig. 6), we can see that the emission is partially optically thick up to $\nu = 47$ GHz, thus, we take this value as a lower limit to the turnover frequency ν_t. As in the case of VLA 1, we also adopt a jet inclination angle $i = 45^\circ$, and estimate lower and upper limits for the mass-loss rate considering different approximations for the ionization fraction and the jet velocity, i.e. $\sim 4 \times 10^{-6}$ M$_\odot$ yr^{-1} (assuming $x_\mathrm{o} = 1$ and $V_\mathrm{jet} = 100$ km s^{-1}) and $\sim 4 \times 10^{-4}$ M$_\odot$ yr^{-1} (assuming $x_\mathrm{o} = 0.1$ and $V_\mathrm{jet} = 1000$ km s^{-1}), respectively. Such mass-loss rates are significantly higher than those estimated in low- and intermediate-mass YSOs (e.g. Beltrán et al. 2001; Anglada et al. 2018), but similar to the values obtained in high-mass YSOs (e.g. Rodríguez et al. 1994; Guzmán et al. 2012; Añez-López et al. 2020), supporting that VLA 3 is excited by a massive protostar.

4.3 Bc and VLA 4

In Fig. 1(c), we show the radio image with the highest resolution and sensitivity to date of Bc and VLA 4. This allows us to resolve their structure, and study the nature of their emission through the spectral index map. The source Bc is clearly resolved into two components (labelled as Bc [E] and Bc [W] in Fig. 1). We note that Bc [W]–Bc [E] form an elongated structure, with its minor axis aligned with the VLA 3 jet direction as we would expect to observe in a bow shock produced by the impact of a supersonic jet with the environment gas (e.g. Tafalla et al. 2017; Castellanos-Ramírez, Raga & Rodríguez-González 2018). This supports the scenario proposed by Carrasco-González et al. (2010) who interpreted Bc as an obscured radio

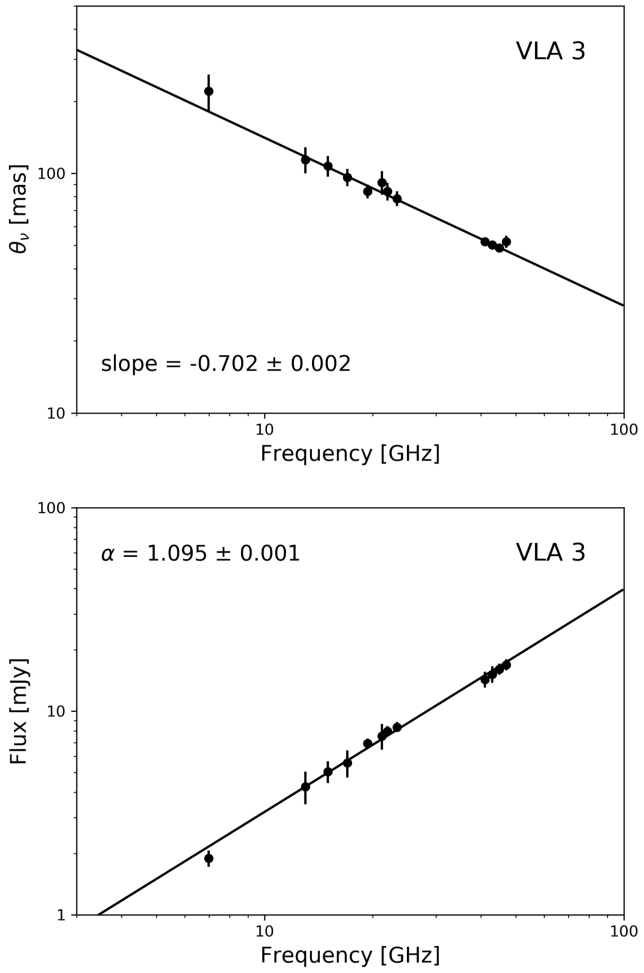

Figure 6. Dependence of the angular size of the jet with frequency (top panel) and SED (bottom panel) of VLA 3. Flux densities and semimajor axes θ_ν, are obtained from Gaussian fits to the brightness profile of VLA 3, in 2 GHz bandwidth images. To measure flux densities, we use uniform-weighted images (*C* band) and natural-weighted images (*Ku*, *K*, and *Q* bands), while angular sizes were measured in uniform-weighted images (*C*, *Ku*, and *K* bands) and Briggs-weighted (robust -1) images (Q band). Solid lines are linear least-squares fits to the log data. Angular size error bars correspond to fitting errors, while flux error bars consider both fitting and calibration errors.

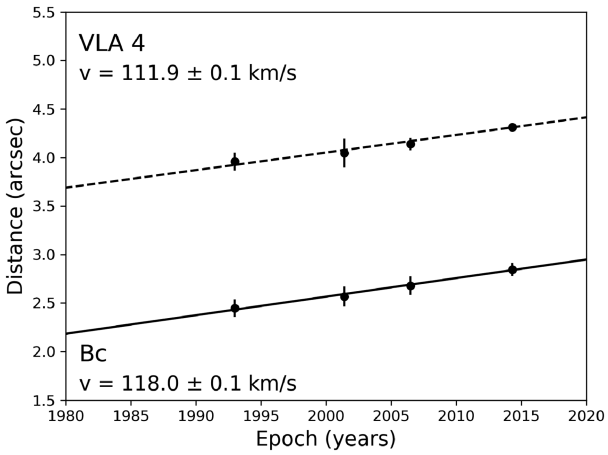

Figure 7. Proper motion diagrams for the Bc and VLA 4 sources. Positions are computed as the distances to the averaged coordinates of the system VLA 1–VLA 2–VLA 3 in four epochs (1992.98, 2001.40, 2006.47, and 2014.29): RA(J2000) = $20^{\rm h}38^{\rm m}36\overset{\rm s}{.}47$, Dec(J2000) = $42^\circ37'34\overset{''}{.}15$. The solid lines are least-square fits to the data. Velocities on the plane of sky are derived by assuming a distance to the region of 1.3 kpc (Rygl et al. 2012). Bc and VLA 4 are moving away from the system with PAs of $\sim -20^\circ$ and $\sim -10^\circ$, respectively.

Herbig–Haro (HH) object, possibly excited by the VLA 3 jet. A flattened structure similar to that of Bc is also seen in the frontal region of the shock of the obscured HH 80N object (Rodríguez-Kamenetzky et al. 2019).

Carrasco-González et al. (2010) studied the kinematics of these sources by computing proper motions relative to VLA 3 in three epochs (1992.90, 1998.23, and 2006.38) spanning 13.48 yr. Adopting a distance to the region of 2 kpc (Dickel, Wendker & Bieritz 1969), they derived for Bc a velocity of 220 ± 70 km s^{-1} moving on the plane of the sky, and towards the south, approximately along the major axis of the VLA 3 radio jet. Regarding VLA 4, they suggested it could be either an independent star or shock-excited gas produced by a previous ejection from VLA 3. However, even though they noticed a small displacement of VLA 4 to the south with respect to VLA 3 between 2000 and 2006, they were not able to distinguish between these two scenarios. Regarding this, we measured the proper motion of both sources along a time span of 22 yr, from 1992 to 2014. Positions of the sources in 2014 were measured in the *K*-band image, since it is the highest angular resolution image where Bc and VLA 4 are detected (see Fig. 2). We compute the proper motions relative to the average position of the system VLA 1–VLA 2–VLA 3 assuming it is stationary, instead of VLA 3 only. In this way, we reduce possible errors associated with variations in the shape of VLA 3 due to observational effects (e.g. differences in the beam size at each epoch) or real changes (e.g. new ejections from VLA 3). Although Bc shows substructure, we measure the displacement of the two-component complex. Fig. 7 shows that both Bc and VLA 4 are moving away from the system in the south-east direction (PA $\simeq -20^\circ$ and -10°, individually, see Fig. 7) with velocities on the plane of the sky of 1.9×10^{-2} ($\sim$118 km s^{-1}) and 1.8×10^{-2} arcsec yr^{-1} ($\sim$112 km s^{-1}), respectively (assuming the updated distance to the region of 1.3 kpc; Rygl et al. 2012). The velocity of Bc differs from the value given by Carrasco-González et al. (2010), but this is mostly due to the difference in the adopted distance to the region (considering a distance of 2 kpc we obtain velocities of 170 and 180 km s^{-1} for VLA 4 and Bc, respectively, closer to the results reported by these authors). Thus, the shape and proper motions of Bc and VLA 4 are consistent with both sources tracing shock-excited gas (obscured HH objects). Moreover, from the spectral index map (Fig. 1c) we see that Bc and VLA 4 are dominated by flat spectral indices ($\alpha \sim 0$), as it would be expected for optically thin free–free emission produced by shock-ionized material. Thus, flat spectral indices, together with the shape of the sources, their proper motions, and propagation direction constitute solid evidence supporting the shock scenario.

Among the sources VLA 1, VLA 2, and VLA 3, VLA 1 and VLA 2 have associated outflows along the north-east–south-west direction (e.g. Torrelles et al. 1997, 2003; Carrasco-González et al. 2015). Therefore, VLA 3 is the only source elongated in the north-west–south-east direction (PA $\simeq -17^\circ$), consistent with the direction of the proper motions of Bc and VLA 4 (PA $\simeq -20^\circ$ and -10°). This, along with the results found in Section 4.2, suggests that VLA 3 is the driving source of Bc and VLA 4. In addition, the fact that Bc and VLA 4 are not associated with any

of the detected millimetre cores (see Section 3.2; Fig. 3) suggest that they are not protostars, further supporting our shock-excited gas interpretation for these sources. This kind of obscured HH objects, exhibiting proper motions higher than 100 km s^{-1}, have also been observed in radio continuum in other intermediate- and high-mass star-forming regions: e.g. Serpens (Curiel et al. 1993; Rodríguez-Kamenetzky et al. 2016), GGD 27 (Martí, Rodríguez & Reipurth 1995, 1998; Masqué et al. 2015; Rodríguez-Kamenetzky et al. 2019), and Cepheus A (Curiel et al. 2006).

5 CONCLUSIONS

We presented an analysis of high-sensitivity, high-resolution multifrequency VLA observations of the massive star-forming region W75N (B), together with complementary studies performed with ALMA and VLA archive data. Our study leads us to the following conclusions:

(i) VLA 1 is detected at all the observed frequencies (4–48 GHz). Its SED over the entire range of frequencies is consistent with thermal free–free emission from an HCH II region ($\lesssim$1 arcsec, $\lesssim$1300 au), while the high angular resolution spectrum of the most compact component at high frequencies (40–48 GHz) is compatible with a thermal radio jet at scales of $\approx$0.1 arcsec ($\approx$130 au), with a spectral index $\alpha \approx +0.5$ ($S_\nu \propto \nu^\alpha$). This suggests that VLA 1 is driving a thermal radio jet, and it is likely at the early stage of the photoionization.

(ii) VLA 3 shows an elongated structure at scales of few tenths of arcsec (few hundred of au), with its major axis oriented in the north-west–south-east direction (PA $\approx -17^\circ$). Both the SED and the size dependence with frequency indicate that this source is also driving a thermal radio jet.

(iii) We computed proper motions of the radio continuum sources Bc and VLA 4 in a time interval of 22 yr. We found both sources are moving away towards the south, in a similar direction as the VLA 3 thermal radio jet, with velocities of $\approx$112–118 km s^{-1} ($\approx$1.8–1.9 $\times$ 10^{-2} arcsec yr^{-1}). From the SED analysis we found these sources are dominated by flat spectral indices, as it is expected for optically thin free–free emission produced by shock-ionized material. These results support the scenario in which Bc and VLA 4 are obscured HH objects tracing shocks of the jet driven by VLA 3.

(iv) Four 1.3 mm continuum cores are observed with ALMA (MM1, MM2, MM3, and MM[N]) in a region of $\sim$14 arcsec. Three of these millimetre cores, MM1, MM2, and MM3, had previously been identified with the SMA interferometer, while MM[N] had not been previously reported. VLA 1, VLA 2, and VLA 3 are associated with the brightest core MM1. Bc and VLA 4 are not associated with any of the millimetre continuum cores, supporting they are not YSOs but shock-excited gas as concluded from our VLA observations.

(v) We have detected three new weak compact radio continuum sources (VLA[SW], VLA[NE], and Bd). Two of them, VLA[SW] and VLA[NE] are associated with the millimetre cores MM2 and MM3, respectively, suggesting they are embedded YSOs belonging to the W75N (B) massive star-forming region.

(vi) With our VLA observations, we have identified a cluster of at least five YSOs (VLA 1, VLA 2, VLA 3, VLA[SW], and VLA[NE]) in a region of $\sim$10 arsec ($\sim$13 000 au). All of the sources for which information was obtained on their structure and SED, exhibit accretion/outflow activity at different relative stages of their evolution. In this sense, given that VLA 1 has indications that it has already started the photoionization stage, it could be relatively more evolved than VLA 2 and VLA 3. To further characterize this cluster of YSOs, ALMA observations with very high angular resolution are needed to resolve individually the gas/dust content of each YSO, as well as to study their expected different chemical compositions.

ACKNOWLEDGEMENTS

We thank our anonymous referee for her/his very valuable comments and suggestions on the manuscript. The work of AR-K and CC-G was supported by Universidad Nacional Autónoma de México DGAPA-PAPIIT grant number IN108218. JC acknowledges support from grant PAPIIT-UNAM-IG100218. AR-K thanks the Consejo Nacional de Investigaciones Científicas y Técnicas (CONICET) to support postdoctoral research. AR-K and JMT acknowledge support from the European Union's Horizon 2020 Research and Innovation program under the Marie Sklodowska-Curie grant agreement number 734374 – Project acronym: LACEGAL. NA-L, JFG, and JMT are supported by the Spanish grant AYA2017-84390-C2-R (AEI/FEDER, UE). SC acknowledges support from DGAPA, UNAM and CONACYT, México. JFG acknowledges financial support from the State Agency for Research of the Spanish Ministerio de Ciencia, Innovación y Universidades (MCIU) through the 'Center of Excellence Severo Ochoa' award for the Instituto de Astrofísica de Andalucía (SEV-2017-0709). This paper makes use of the following ALMA data: ADS/JAO.ALMA 2017.1.01593.S. ALMA is a partnership of ESO (representing its member states), NSF (USA) and NINS (Japan), together with NRC (Canada), MOST and ASIAA (Taiwan), and KASI (Republic of Korea), in cooperation with the Republic of Chile. The Joint ALMA Observatory is operated by ESO, AUI/NRAO and NAOJ.

DATA AVAILABILITY

The data sets underlying this article were derived from sources in the public domain: NRAO Data Archive, https://science.nrao.edu/observing/data-archive.

REFERENCES

Añez-López N. et al., 2020, ApJ, 888, 41
Anglada G., Rodríguez L. F., Carrasco-González C., 2018, A&AR, 26, 3
Baart E. E., Cohen R. J., Davies R. D., Norris R. P., Rowland P. R., 1986, MNRAS, 219, 145
Beltrán M. T., Estalella R., Anglada G., Rodríguez L. F., Torrelles J. M., 2001, AJ, 121, 1556
Beltrán M. T., Cesaroni R., Moscadelli L., Sánchez-Monge Á., Hirota T., Kumar M. S. N., 2016, A&A, 593, A49
Briggs D. S., 1995, American Astronomical Society Meeting Abstracts #187, p. 112.02
Carrasco-González C., Rodríguez L. F., Torrelles J. M., Anglada G., González-Martín O., 2010, AJ, 139, 2433
Carrasco-González C. et al., 2015, Science, 348, 114
Castellanos-Ramírez A., Raga A. C., Rodríguez-González A., 2018, ApJ, 867, 29
Colom P., Lekht E. E., Pashchenko M. I., Rudnitskii G. M., Tolmachev A. M., 2018, Astron. Rep., 62, 440
Curiel S., Rodríguez L. F., Moran J. M., Cantó J., 1993, ApJ, 415, 191
Curiel S. et al., 2006, ApJ, 638, 878
Davis C. J., Moriarty-Schieven G., Eislöffel J., Hoare M. G., Ray T. P., 1998, AJ, 115, 1118
Dickel H. R., Wendker H., Bieritz J. H., 1969, A&A, 1, 270
Dickel J. R., Dickel H. R., Wilson W. J., 1978, ApJ, 223, 840

Guzmán A. E., Garay G., Brooks K. J., Voronkov M. A., 2012, ApJ, 753, 51
Guzmán A. E., Garay G., Rodríguez L. F., Contreras Y., Dougados C., Cabrit S., 2016, ApJ, 826, 208
Hunter T. R., Taylor G. B., Felli M., Tofani G., 1994, A&A, 284, 215
Hutawarakorn B., Cohen R. J., Brebner G. C., 2002, MNRAS, 330, 349
Kim J.-S. et al., 2013, ApJ, 767, 86
Krasnov V. V., Lekht E. E., Rudnitskii G. M., Pashchenko M. I., Tolmachev A. M., 2015, Astron. Lett., 41, 517
Kurtz S., 2005, in Cesaroni R., Felli M., Churchwell E., Walmsley M., eds, Proc. IAU Symp. 227, Massive Star Birth: A Crossroads of Astrophysics. Kluwer, Dordrecht, p. 111
Martí J., Rodríguez L. F., Reipurth B., 1995, ApJ, 449, 184
Martí J., Rodríguez L. F., Reipurth B., 1998, ApJ, 502, 337
Masqué J. M., Rodríguez L. F., Araudo A., Estalella R., Carrasco-González C., Anglada G., Girart J. M., Osorio M., 2015, ApJ, 814, 44
McMullin J. P., Waters B., Schiebel D., Young W., Golap K., 2007, in Shaw R. A., Hill F., Bell D. J., eds, ASP Conf. Ser. Vol. 376, Astronomical Data Analysis Software and Systems XVI. Astron. Soc. Pac., San Francisco, p. 127
Minh Y. C., Su Y. -N., Chen H. -R., Liu S. -Y., Yan C. -H., Kim S. -J., 2010, ApJ, 723, 123
Minier V., Booth R. S., Conway J. E., 2000, A&A, 362, 1093
Persi P., Tapia M., Smith H. A., 2006, A&A, 445, 971
Rau U., Cornwell T. J., 2011, A&A, 532, 71
Reynolds S. P., 1986, ApJ, 304, 713
Rodríguez L. F., Garay G., Curiel S., Ramírez S., Torrelles J. M., Gḿez Y., Velázquez A., 1994, ApJ, 430, L6
Rodríguez-Kamenetzky A., Carrasco-González C., Araudo A. T., Torrelles J. M., Anglada G., Martí J., Rodríguez L. F., Valotto C., 2016, ApJ, 818, 27
Rodríguez-Kamenetzky A., Carrasco-González C., González-Martín O., Araudo A. T., Rodríguez L. F., Vig S., Hofner P., 2019, MNRAS, 482, 4687
Rygl K. L. J. et al., 2012, A&A, 539, A79
Shepherd D. S., Testi L., Stark D. P., 2003, ApJ, 584, 882
Shepherd D. S., Kurtz S. E., Testi L., 2004, ApJ, 601, 952
Surcis G., Vlemmings W. H. T., Dodson R., van Langevelde H. J., 2009, A&A, 506, 757
Surcis G., Vlemmings W. H. T., Curiel S., Hutawarakorn Kramer B., Torrelles J. M., Sarma A. P., 2011, A&A, 527, A48
Surcis G. et al., 2014, A&A, 565, L8
Tafalla M. et al., 2017, A&A, 597, 119
Torrelles J. M., Gómez J. F., Rodríguez L. F., Ho P. T. P., Curiel S., Vázquez R., 1997, ApJ, 489, 744
Torrelles J. M. et al., 2003, ApJ, 598, L115

APPENDIX: SUPPLEMENTARY TABLES AND FIGURES

Table A1 lists the parameters of the images used in this paper. The columns are as follows: (1) spectral band, (2) epoch of observation, (3) central frequency, (4) bandwidth, (5) weighting of visibilities (NA = natural, UN = uniform, and R0 and R-1 = Briggs, using robust parameter equal to 0 and −1), (6) synthesized beam size and position angle, (7) rms noise, and (8) Figure/Table in which each image is used in the paper.

Fig. A1 shows a radio continuum map of the region, with close-ups of the three new compact sources of <100 μJy detected in the field: VLA[NE], VLA[SW], and Bd.

Table A1. Parameters of the VLA images.

Spectral band	Epoch	Central frequency (GHz)	Total bandwidth (GHz)	Weighting	Synthesized beam	Rms (μJy per beam)	Used in
X	1992.90	8.44	0.1	R0	0.″23 × 0.″19; −56°	90	Fig. 7
Ku	2001.31	15.0	0.1	R0	0.″47 × 0.″39; −83°	80	Fig. 7
X	2006.38	8.46	0.1	R0	0.″22 × 0.″17; 18°	50	Fig. 7
C	2014.29	6.0	4.0	UN	0.″28 × 0.″20; 83°	30	Fig. 2, Table 2
Ku	2014.29	15.0	6.0	NA	0.″21 × 0.″16; −75°	10	Figs 2, 4, Table 2
K	2014.29	22.0	8.5	NA	0.″16 × 0.″10; −74°	10	Figs 2, 4, 7, Table 2
K	2014.29	22.0	8.5	R0	0.″15 × 0.″07; −77°	10	Table 3
Q	2014.29	44.0	10.0	NA	0.″07 × 0.″05; −29°	20	Figs 2, 4, Table 2
Q	2014.29	44.0	10.0	UN	0.″04 × 0.″05; −9°	100	Fig. 4
C + *Ku* + *K* + *Q*	2014.29	25.9	28.5	R0	0.″12 × 0.″09; −69°	8	Figs 1, A1, Table 2
C	2014.29	5.0	2.0	UN	0.″37 × 0.″37; 0°	90	Fig. 5
C	2014.29	7.0	2.0	UN	0.″37 × 0.″37; 0°	90	Fig. 5
C	2014.29	7.0	2.0	UN	0.″27 × 0.″20; 87°	50	Fig. 6
Ku	2014.29	13.0	2.0	NA	0.″37 × 0.″37; 0°	90	Fig. 5
Ku	2014.29	13.0	2.0	NA	0.″26 × 0.″19; −85°	45	Fig. 6
Ku	2014.29	13.0	2.0	UN	0.″17 × 0.″11; 90°	120	Fig. 6
Ku	2014.29	15.0	2.0	NA	0.″37 × 0.″37; 0°	100	Fig. 5
Ku	2014.29	15.0	2.0	NA	0.″20 × 0.″15; −77°	35	Fig. 6
Ku	2014.29	15.0	2.0	UN	0.″15 × 0.″09; 89°	100	Fig. 6
Ku	2014.29	17.0	2.0	NA	0.″37 × 0.″37; 0°	100	Fig. 5
Ku	2014.29	17.0	2.0	NA	0.″18 × 0.″14; −66°	30	Fig. 6
Ku	2014.29	17.0	2.0	UN	0.″13 × 0.″09; −87°	90	Fig. 6
K	2014.29	19.4	2.0	NA	0.″37 × 0.″37; 0°	90	Fig. 5
K	2014.29	19.4	2.0	NA	0.″18 × 0.″11; −74°	20	Fig. 6
K	2014.29	19.4	2.0	UN	0.″13 × 0.″07; −84°	75	Fig. 6
K	2014.29	21.2	2.0	NA	0.″37 × 0.″37; 0°	100	Fig. 5
K	2014.29	21.2	2.0	NA	0.″17 × 0.″10; −75°	20	Fig. 6
K	2014.29	21.2	2.0	UN	0.″12 × 0.″063; −84°	160	Fig. 6
K	2014.29	22.0	2.0	NA	0.″37 × 0.″37; 0°	150	Fig. 5
K	2014.29	22.0	2.0	NA	0.″15 × 0.″09; −73°	30	Fig. 6
K	2014.29	22.0	2.0	UN	0.″10 × 0.″054; −85°	130	Fig. 6
K	2014.29	23.4	2.0	NA	0.″37 × 0.″37; 0°	120	Fig. 5
K	2014.29	23.4	2.0	NA	0.″15 × 0.″10; −74°	20	Fig. 6
K	2014.29	23.4	2.0	UN	0.″11 × 0.″056; −84°	90	Fig. 6
Q	2014.29	41.0	2.0	NA	0.″37 × 0.″37; 0°	220	Fig. 5
Q	2014.29	41.0	2.0	NA	0.″08 × 0.″056; −40°	30	Fig. 6
Q	2014.29	41.0	2.0	R-1	0.″04 × 0.″039; 82°	70	Fig. 6
Q	2014.29	43.0	2.0	NA	0.″37 × 0.″37; 0°	200	Fig. 5
Q	2014.29	43.0	2.0	NA	0.″07 × 0.″05; −27°	30	Fig. 6
Q	2014.29	43.0	2.0	R-1	0.″04 × 0.″039; 7°	80	Fig. 6
Q	2014.29	45.0	2.0	NA	0.″37 × 0.″37; 0°	300	Fig. 5
Q	2014.29	45.0	2.0	NA	0.″07 × 0.″05; −25°	40	Fig. 6
Q	2014.29	45.0	2.0	R-1	0.″04 × 0.″038; −13°	100	Fig. 6
Q	2014.29	47.0	2.0	NA	0.″37 × 0.″37; 0°	350	Fig. 5
Q	2014.29	47.0	2.0	NA	0.″09 × 0.″05; −18°	70	Fig. 6
Q	2014.29	47.0	2.0	R-1	0.″06 × 0.″037; −19°	200	Fig. 6
Q	2014.29	40.5	1.0	R0	0.″05 × 0.″043; −53°	50	Fig. 5
Q	2014.29	41.5	1.0	R0	0.″05 × 0.″043; −36°	50	Fig. 5
Q	2014.29	42.5	1.0	R0	0.″05 × 0.″042; −24°	55	Fig. 5
Q	2014.29	43.5	1.0	R0	0.″05 × 0.″042; −7°	65	Fig. 5
Q	2014.29	44.5	1.0	R0	0.″05 × 0.″040; −25°	65	Fig. 5
Q	2014.29	45.5	1.0	R0	0.″05 × 0.″039; −20°	80	Fig. 5
Q	2014.29	46.5	1.0	R0	0.″06 × 0.″039; −20°	100	Fig. 5
Q	2014.29	47.5	1.0	R0	0.″08 × 0.″040; −16°	180	Fig. 5

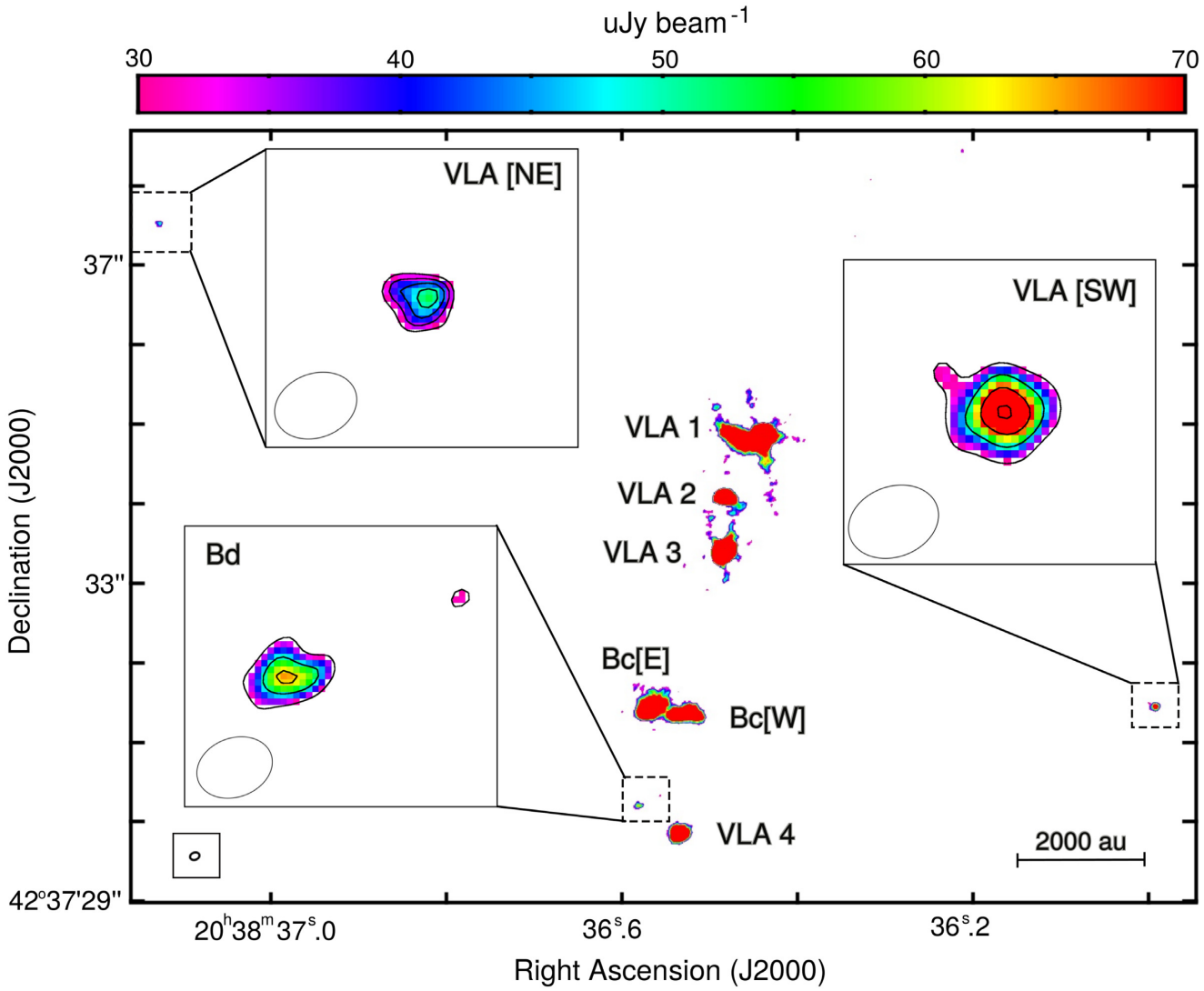

Figure A1. Radio continuum image of W75N (B) made by the combination of *C*, *Ku*, *K*, and *Q* bands (epoch 2014.29), using multifrequency synthesis cleaning and Briggs weighting (robust 0). Three new weak (<100 μJy) compact radio continuum sources are detected: VLA[NE] and VLA[SW] located at ∼8 arcsec north-east and ∼6 arcsec south-west from VLA 2, respectively, and Bd at ∼0.5 arcsec north-east from VLA 4. Countour levels correspond to 4, 5, 6, and 7 times 7×10^{-6} Jy beam^{-1} (VLA[NE]); 4, 7, 10, and 13 times 7×10^{-6} Jy beam^{-1} (VLA[SW]); and 4, 7, and 9 times 7×10^{-6} Jy beam^{-1} (Bd). Black rectangles show zoomed-in regions enclosing each of the new sources, where the physical scale is given by the synthesized beam, corresponding to 160 au × 120 au (PA $= -69°$), approximately.

This paper has been typeset from a TEX/LATEX file prepared by the author.